Editors' Suggestion | Featured in Physics

Temporal Refraction in an Acoustic Phononic Lattice

Brian L. Kim,[1] Christopher Chong,[2] and Chiara Daraio[1,*]
[1]Department of Mechanical and Civil Engineering, California Institute of Technology, Pasadena, California 91125, USA
[2]Department of Mathematics, Bowdoin College, Brunswick, Maine 04011, USA

(Received 2 June 2023; accepted 21 June 2024; published 15 August 2024)

In this Letter, we present the first experimental demonstration of the temporal refraction of acoustic waves in a phononic lattice. A step change in grounding stiffness results in a discontinuous change in group velocity across a so-called temporal boundary. This leads to frequency translation of incident signals, which maintain constant wavelength. We use the system to construct phononic analogs of the classical Snell and Fresnel relationships for temporal boundaries, providing evidence of temporal refraction. Last, we propose the ability to design systems to achieve tunable slow sound.

DOI: 10.1103/PhysRevLett.133.077201

Introduction—Propagation of waves in time-varying media has received much attention across a variety of domains. Previous work in both electromagnetic and mechanical systems has focused on periodic variations in medium properties, enabling phenomena including parametric amplification [1–3], nonreciprocal propagation [4–7], or topological effects [8–10]. Recent focus has shifted to the interaction of propagating waves with nonperiodic temporal variations, especially boundaries or discontinuities of the properties of a medium, specifically the refractive index, in time [11–13]. Since temporal boundaries were introduced [14], they have been studied as a temporal analog to spatial refraction [15–22] and extended to general space-time variations [23–26].

Various functionalities enabled by rapid time-variation have been proposed for electromagnetic waves, such as antireflection temporal coatings [27], thin absorbers [28], or time mirrors [29,30]. Natural extensions of temporal boundaries have been explored, including temporal slabs and layered media [31–34] and boundaries with finite rise times [35]. Temporal boundaries can enable broadband, linear frequency conversion [12,13] without the typical considerations of conventional nonlinear frequency conversion, such as phase matching [36–39]. Experimentally, flash ionization [40,41], rapidly time-varying optical metasurfaces [12], ultrafast pumping of metal-semiconductor waveguides [42], and electrostriction-controlled water waves [43] have been shown to achieve frequency conversion using temporal boundaries. Crucially, achieving temporal boundaries typically requires either the uniform change of an external field [40,41,43] or precise coincidence of pumping and input signals [12].

In this Letter, we present the first experimental demonstration of the refraction of acoustic waves across a temporal boundary in elastic properties. We employ a one-dimensional phononic lattice composed of repelling magnets (serving as discrete masses and springs) controlled by electromagnetic coils (serving as grounding stiffness elements), see Fig. 1(a). The temporal boundary, depicted in Fig. 1(b), is realized by a rapid, steplike change in grounding stiffness, as shown in Fig. 1(c). The measured conversion of frequency, conservation of wavelength, and transmission and reflection of signals provide evidence of temporal refraction in acoustic and elastic systems and support the proposed realization of tunable slow sound. This novel phononic demonstration bolsters the potential for the implementation of temporal refraction in similar acoustic and elastic devices and, moreover, highlights the versatility of discrete systems for implementing the dynamic modulation necessary to realize temporal boundaries in any domain.

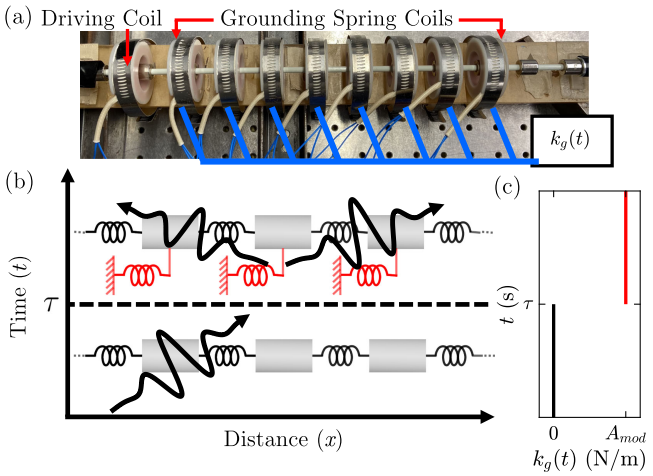

FIG. 1. (a) Photo of experimental lattice, driving, and grounding stiffness coils labeled. (b) Schematic of lattice before (below) step-up temporal boundary ($t < \tau$) with depiction of incident wave, and after (above) the temporal boundary ($t > \tau$) with transmitted and reflected waves observed. (c) Step-up grounding stiffness, from $k_g(t) = 0$ to $k_g(t) = A_{\mathrm{mod}}$ at temporal boundary τ.

*Contact author: daraio@caltech.edu

Lattice model—The lattice depicted in Fig. 1(a) is modeled as a discrete mass-spring chain, similar to prior work [5,44]. The equation of motion for the nth mass (ring magnet) with displacement u_n (m) is written

$$m\frac{d^2u_n}{dt^2}+c\frac{du_n}{dt}+k_{g,n}(t)u_n+k_{\mathrm{lin}}\Delta u=F_{dr,n}(t), \quad (1)$$

for $n=1$ to 12, with fixed boundary conditions $u_1(t)=u_{12}(t)=0$ and where $\Delta u=(2u_n-u_{n-1}-u_{n+1})$. All ring magnets have mass $m=9.8$ g. The damping coefficient $c=0.15\ \mathrm{N\,s\,m^{-1}}$ is determined empirically by matching measured and simulated spatial decay of traveling waves (see Supplemental Material [45]). $k_{\mathrm{lin}}=87.03\ \mathrm{N\,m^{-1}}$ is a linear fit of measured coupling stiffness between adjacent masses [44]. For a temporal boundary, the grounding stiffness takes the form

$$k_{g,n}(t)=\begin{cases}\delta_{j,n}A_0, & t<\tau\\ \delta_{j,n}A_1, & t\geq\tau\end{cases} \quad (2)$$

so the masses experience a discontinuous change in grounding stiffness at time τ. We consider a "step-up," where $A_0=0$ and $A_1=A_{\mathrm{mod}}$ (depicted in Fig. 1(c)), and "step-down," where $A_0=A_{\mathrm{mod}}$ and $A_1=0$ ($[A_{\mathrm{mod}}]=\mathrm{N\,m^{-1}}$). To preserve symmetry in the experimental lattice, Kronecker delta with index $j=3$ to 10 applies only to masses with grounding stiffness coils; the lack of grounding stiffness at $n=2$ and 11 does not affect the spatial or temporal spectral content of signals (see Supplemental Material [45]). The driving force $f_{dr,n}=A_{dr}\delta_{2,n}g(t)$, has driving amplitude $A_{dr}([A_{dr}]=N)$, and Kronecker delta $\delta_{2,n}$ applies input forcing only to mass $n=2$. For all measurements and simulations a Gaussian modulated sinusoidal pulse of the form $g(t)=\exp[-(t-t_0)^2/(2\sigma^2)]\cos(2\pi f_{dr}t)$ is utilized where f_{dr} is the center frequency of the pulse, $t_0=1.3/(B_{-6\,\mathrm{dB}}f_{dr})$, $\sigma=\sqrt{2\log 2}/(\pi B_{-6\,\mathrm{dB}}f_{dr})$ and $B_{-6\,\mathrm{dB}}=0.6$.

Temporal analog of Snell's law and Fresnel relations—For initial data spectrally concentrated at wave number k_0 the resulting incident wave can be approximated by $u_n(t)=U_ie^{i(k_0n+\omega_0(k_0)t)}$ for $t<\tau$ where U_i is the amplitude of the incident wave and $\omega_0(k)^2=A_0/m+4k_{\mathrm{lin}}\sin^2(k/2)/m$. For $t>\tau$, the solution can be approximated by $u_n(t)=U_te^{i[k_0n+\omega_1(k_0)t]}+U_re^{i[k_0n-\omega_1(k_0)t]}$ where U_t and U_r are the amplitude of the transmitted and reflected wave, respectively, and $\omega_1(k)^2=A_1/m+4k_{\mathrm{lin}}\sin^2(k/2)/m$ [see Fig. 2(a) for step-up case]. Differentiating the two dispersion relationships $\omega_0(k)^2$ and $\omega_1(k)^2$ with respect to k leads to

$$\omega_0(k)\omega_0'(k)=2k_{\mathrm{lin}}/m\sin(k/2)\cos(k/2), \quad (3)$$

$$\omega_1(k)\omega_1'(k)=2k_{\mathrm{lin}}/m\sin(k/2)\cos(k/2), \quad (4)$$

which implies that

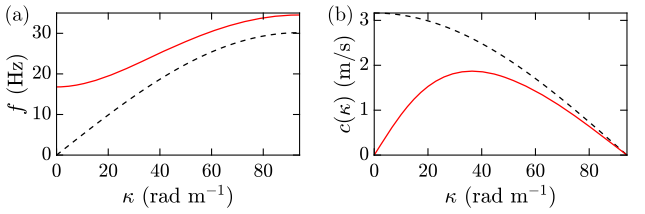

FIG. 2. (a) Dispersion relation of infinite lattice before (black dashed) and after (red solid) step-up grounding stiffness temporal boundary [$\kappa=k/a$, $f=\omega/(2\pi)$ are dimensional wave number (rad m^{-1}) and frequency (Hz), respectively]. (b) Group velocity versus wave number of infinite lattice before (black dashed) and after (red solid) step-up boundary.

$$\delta\coloneqq\frac{\omega_0(k)}{\omega_1(k)}=\frac{c_1(k)}{c_0(k)}, \quad (5)$$

where the group velocities are $c_0(k)=\omega_0'(k)$ and $c_1(k)=\omega_1'(k)$, respectively, [see Fig. 2(b)]. Equation (5) is a phononic analog of Snell's law for time refraction. Corresponding Fresnel relations are found by enforcing continuity at the interface $t=\tau$, yielding

$$\frac{\tilde{U}_t}{\tilde{U}_i}=\frac{1+\delta}{2}, \quad (6a)$$

$$\frac{\tilde{U}_r}{\tilde{U}_i}=\frac{1-\delta}{2}, \quad (6b)$$

where $\tilde{U}_i=U_ie^{i\omega_0(k_0)\tau}$, $\tilde{U}_t=U_te^{i\omega_1(k_0)\tau}$, $\tilde{U}_r=U_re^{i\omega_1(k_0)\tau}$. Equation (6b) implies there will always be a reflected wave unless $\delta=1$, which corresponds to the case of no temporal change in grounding stiffness ($A_{\mathrm{mod}}=0$). More details on the derivation of the above Snell's and Fresnel relations are given in the Supplemental Material [45].

Experimental observation of temporal refraction—The experimental platform is adapted from [5,44] (see Ref. [45]). The one-dimensional mass-spring chain comprises N ring magnets sliding on a rigid rod. Adjacent masses have opposite polarity, resulting in a repulsive force that acts as the coupling springs. Grounding springs are implemented using electromagnetic coils fixed concentrically around the equilibrium positions of each mass. A restoring force on each mass proportional to an applied current provides an effective grounding stiffness. The chain has fixed boundary conditions, and a driving electromagnetic coil is offset axially from the equilibrium position of the first nonfixed mass on one end. Figure 1(a) shows a photograph of the experimental lattice, with the driving coil and grounding spring coils indicated. Large frictional losses limit the experimental lattice to $N=12$ masses.

We first demonstrate that the proposed lattice with a temporal boundary can efficiently convert input frequency. We consider Gaussian-modulated sinusoidal pulses incident on a temporal boundary. For the step-up, we target

center frequencies (f_{dr}) between 10 and 30 Hz, in 2 Hz increments. We do not consider lower frequencies because at $f_{dr} < 10$ Hz the incident wavelength exceeds the length of the lattice, which is limited by the presence of friction (see Supplemental Material [45]). For the step-down incident frequencies, we use wave packets of the same wavelengths as the step-up, which are the postboundary frequencies $f_1 = \omega_1(k_0)/(2\pi)$ of the step-up case. At the temporal boundary $\tau = 0.17255$ s, a dc voltage applied to the modulating coils is turned on (off) for a step-up (step-down) boundary, resulting in an rapid change in grounding stiffness of the modulated portion of the lattice from $k_g(t<\tau) = A_0\,\mathrm{N\,m^{-1}}$ to $k_g(t\geq\tau) = A_1\,\mathrm{N\,m^{-1}}$ with a change in amplitude of $A_{\mathrm{mod}} \approx 106\,\mathrm{N\,m^{-1}}$ (see Supplemental Material [45]). The velocity time series of every mass ($n = 2$ to $n = 11$) is measured using a laser Doppler vibrometer (see Supplemental Material [45]). Figure 3(a) shows a representative measurement of a velocity time series of the input ($n = 2$) and output ($n = 11$) masses for a step-up boundary.

Input frequency f_0 and output frequency f_1 are defined as the location of the spectral peaks (Fourier transform) of the input and output velocity time series, respectively. The input velocity time series is measured at $n = 2$ for time $t = 0$ to $t = \tau$ to isolate the incident wave packet, and the output velocity time series is measured at $n = 11$ from $t = \tau = 0.17255$ s to $t = t_{\mathrm{max}} \in [0.3, 0.36]$ s to isolate the transmitted wave packet. Typical spectral peaks used to determine f_0 and f_1 are shown in Fig. 3(b), which correspond to the velocity time series shown in Fig. 3(a). Similarly, the wave packet reflected by the temporal boundary is observed by measuring the velocity time series at $n = 2$ from $t = \tau$ to $t = t_{\mathrm{max}}$. Distinguishing temporal reflections from spatial reflections depends on an appropriate choice of t_{max} (see Supplemental Material [45]).

Figure 3(c) shows measured output frequency f_1 versus input frequency f_0 with (step-up, red; step-down, magenta) and without (black) temporal boundaries. Markers (step-up, triangles; step-down, down-triangles; no boundary, circles) show averages for both input and output frequencies with error bars denoting standard error of six sets of measurements. Solid red and magenta curves are the expected output frequency f_1 for the step-up and step-down, respectively, and dashed black is the case of no boundary. Expected output frequency is calculated by rearranging Eq. (5) and substituting $\omega_{0,1} = 2\pi f_{0,1}$, so that $f_1 = f_0 c_0/c_1$. Theoretical propagation speeds c_0 and c_1 are a function of coupling stiffness k_{lin} and magnitude of grounding stiffness $k_{g,n}(t)$. In the absence of the temporal boundary, $f_1 = f_0$, and no frequency conversion is observed. Measured output frequencies after a temporal boundary show excellent agreement with theoretical predictions, especially the step-up, except at higher frequencies approaching the cutoff frequency of the lattice. The step-down suffers from stronger dispersion of incident signals but still exhibits

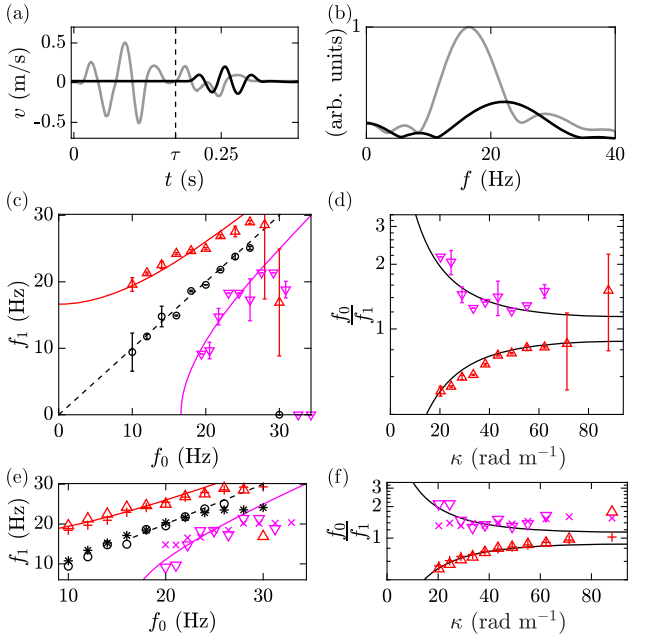

FIG. 3. (a) Representative measured velocity time series of input mass ($n = 2$, gray) and output mass ($n = 11$, black) for Gaussian pulse with center frequency $f_0 = f_{dr} = 18$ Hz. Black dashed line denotes step-up temporal boundary. (b) Fourier transforms of incident (gray) and transmitted signals (black) from (a), showing frequency conversion. (c) Markers with error bars show output frequency versus input frequency of Gaussian pulse signals in lattice with temporal boundary (step-up, red triangles; step-down, magenta down-triangles) and without temporal boundary (black circles). Theoretical curves based on dispersion relationships with (step-up, red; step-down, magenta) and without (dashed black) temporal boundary. (d) Measured ratio of input to output frequency, step-up (red triangles) and step-down (magenta down-triangles), with theoretical phononic analog of Snell's law (black). (e),(f) Comparison of experimental measurement [same data as (c) and (d)] to simulation of frequency conversion and ratio (step-up, crosses; step-down, X's; no boundary, stars).

clear conversion of frequency compared to the lattice without any temporal boundary. Additionally, we plot the measured ratio $\delta = f_0/f_1$ of signals refracted across the temporal boundary as a function of theoretical incident wave number [see Fig. 3(d)], demonstrating that frequency conversion agrees with the analytical prediction based on the phononic analog of Snell's law [Eq. (5)]. Experimental frequency conversion and ratio are compared with the same results for a numerically simulated lattice in Figs. 3(e) and 3(f), solving Eq. (1) using a variable step 4th order Runge-Kutta method (MATLAB ode45) to validate our finite, linear theoretical model.

We now demonstrate the conservation of wavelength across the temporal boundary. Taking a two-dimensional Fourier transform of the velocity field of the lattice before and after the temporal boundary, we determine the frequency and wave number of propagating wave packets as the location of the maximum amplitude in the inverse

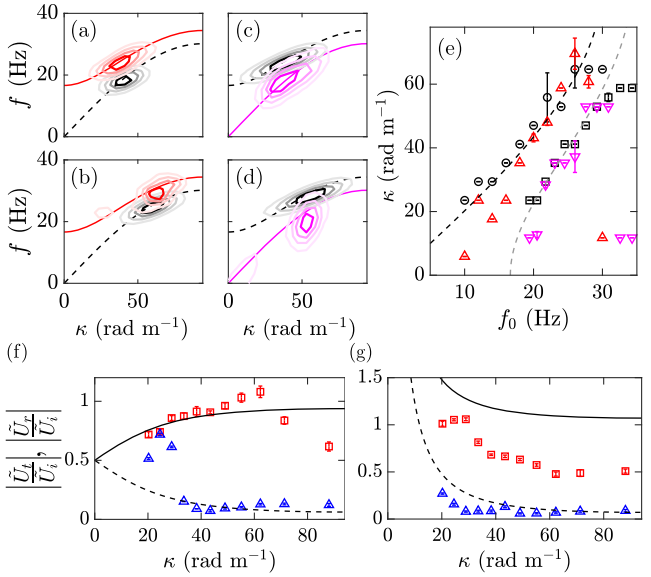

FIG. 4. (a)–(d) Two-dimensional Fourier transform of incident (black contours) and transmitted wave packets for step-up [red contours in (a),(b)] and step-down [magenta contours in (c),(d)] system for input frequencies $f_0 = 18$ (a), $f_0 = 26$ (b), $f_0 = 24.5$ (c), $f_0 = 30.9$ Hz (d). Initial (dashed black) and postboundary (step-up red, step-down magenta) theoretical dispersion relations also shown. (e) Measured step-up and step-down wave number versus input frequency of incident (black circles, squares) and transmitted (red triangles, magenta down-triangles) wave packets with standard error. Theoretical expected wave number for step-up (dashed black) and step-down (dashed gray) also shown. (f),(g) Experimental measurement of Fresnel relations for step-up (f) and step-down (g) boundaries. Amplitude ratios of transmitted to incident wave packets (red squares) and reflected to incident wave packets (blue triangles). Theoretical Fresnel relations based on value of δ for temporal boundary for transmitted (solid) and reflected (dashed) waves.

space. This is shown for two example input frequencies, $f_0 = 18$ and 26 Hz in Figs. 4(a) and 4(b), respectively, for the step-up, and $f_0 = 24.5$ and 30.9 Hz in Figs. 4(c) and 4(d), respectively, for the step-down. Before the boundary, we observe a peak (black contours) centered near the input frequency f_0 and located on the initial dispersion relation $\omega_0(k)$ (dashed black) as expected. After the boundary, the red (magenta) peaks are shifted up (down) in the frequency axis for the step-up (step-down), but remain at approximately the same wave number, now aligned with the postboundary dispersion relation $\omega_1(k)$ in solid red (magenta). This is in contrast to spatial refraction, where the peak would translate left (right) in the wave number axis onto the postboundary dispersion relation [16]. In Fig. 4(e), incident and transmitted wave numbers are plotted versus input frequency f_0 for the full range of input frequencies for both the step-up (black squares and red triangles) and step-down (black circles and magenta down-triangles) boundaries. The expected wave number for temporal refraction, which is the initial dispersion relation $\omega_0(k_0)$, is plotted for the step-up (dashed black) and step-down (dashed gray). Discrepancies at longer wavelengths most likely occur since low frequency input signals do not terminate before the temporal boundary; likewise, shorter wavelengths near the cutoff frequency experience strong dispersion. Overall, however, in clear contrast to the conversion of wavelength that would be present across a spatial boundary, the experiments demonstrate the preservation of the expected wavelength across the temporal boundary, complementing Snell's law to complete the temporal analog to spatial refraction.

Last, we experimentally reconstruct the Fresnel relations given in Eqs. (6a) and (6b). Incident wave packet amplitudes (U_i) are measured as the maximum velocity of a mass before the temporal boundary. Likewise, transmitted (U_t), and reflected (U_r) wave packet amplitudes are given by the maximum velocities immediately after the temporal boundary at masses forward (to the right) and backward (to the left), respectively, of the approximate spatial location of the wave packet at the time of the temporal boundary. Measured ratios of these amplitudes are plotted, with error bars denoting standard error of six sets of measurements, in Figs. 4(f) and 4(g) for the step-up and step-down, respectively, along with corresponding magnitudes of the theoretical predictions, based on the ratio δ for the given temporal boundary. Again, outside of smaller wave numbers, where longer signal periods limit measurement of reflections in the short finite lattice, and larger wave numbers approaching the cutoff frequency, the measured transmitted and reflected amplitudes agree well with the theoretical predictions, although the step-down suffers from low transmission. Still, both cases show a dependence on the incident wavelength in agreement with the phononic analog to the Fresnel relations.

Dynamic slow sound—Having shown the accuracy of the lattice model Eq. (1) [Figs. 3(e) and 3(f)], we propose the implementation of dynamically tunable slow sound in a longer ($N = 256$), dissipation-free lattice of the same design. We consider a small wave number ($f_{dr} = 4$ Hz), since contrast in propagation speed across the step-up boundary ($A_{\mathrm{mod}} = 106\ \mathrm{N\,m^{-1}}$) is highest, and postboundary propagation speed is small as $\kappa \to 0$ [Fig. 2(b)]. Transmitted (and reflected) signals see large reduction in group velocity compared to the incident signal, similar to slow light in photonic crystals [46] and slow sound in sonic crystals [47]. A subsequent step-down boundary recovers initial signal frequency and group velocity. Figure 5(a) shows the displacement field of this step-up–step-down cycle. Figure 5(b) shows the same signal simulated as Fig. 5(a) incident on a similar boundary but with realistic damping and decreased time between boundaries $\tau_2 - \tau_1$. Despite loss in amplitude (order 10^{-4}), slowing and release of the incident signal is observed. At $f_{dr} = 4$ Hz, however, the total transmission coefficient across both boundaries is

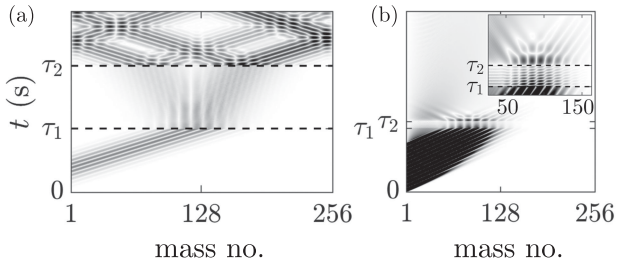

FIG. 5. (a) Normalized displacement magnitude $|u_n(t)|$ (shading intensity) of undamped ($c = 0$), $N = 256$ lattice simulation of small wave number pulse propagating across a step-up boundary at $t = \tau_1$ followed by a step-down boundary at $t = \tau_2$. (b) Scaled $|u_n(t)|$ of damped simulation ($c = 0.15\ \mathrm{N\,s\,m^{-1}}$); inset shows detail at temporal boundaries.

approximately 1.6, which might compensate for losses in potential implementations. While dissipation (and length) limit low-frequency performance in the experimental lattice, the demonstrated temporal control of dispersion might be adapted to other discrete acoustic or elastic systems, for example, higher-Q membrane-based M/NEMS with similar tunable stiffness schemes [48]. Structural complexity, e.g., diatomic arrangements, which is readily adapted in discrete systems, has also been shown theoretically to permit additional control including reversal of signals [49]. As shown, temporal control of dispersion already has the potential to enable dynamically tunable absorption [50] or storing and releasing sound [51]. The ability to modulate discrete elements nonuniformly offers many promising paths to explore additional phenomena less easily implemented in systems where continuous modulation fields are required. Such tuning of medium properties at discrete spatial elements may also extend to metamaterials where implementation of temporal boundaries may allow switchable activation of double-negative, double-zero index, or other exotic effective medium properties [52,53].

Summary and conclusions—We reported the first experimental demonstration of the refraction of acoustic or elastic waves across a temporal boundary. We present the theory of this temporal refraction in a linearized, infinite-length approximation of the experimental lattice, contextualizing experimental results in analogy to the geometrical optics interpretation. This work provides proof of concept for design of acoustic and elastic wave guides and devices with temporal boundaries and rapid changes in group velocity. In particular, implementation of rapid change in stiffness by modulation of discrete elements is potentially scalable and realizable in more complex designs including loss compensation [1,54] or cavity configurations [43], and the band-limited nature of the discrete system considered herein may lead to more stable dynamic responses, since resonances with higher-order modes can be avoided [55].

Acknowledgments—This material is based upon work supported by the U.S. National Science Foundation under Grants No. DGE1745301 (B. L. K.) and No. DMS-2107945 (C. C.). This work was also (partially) supported by the Science and Technology Center New Frontiers of Sound (NewFoS) through NSF Grant No. 2242925 (C. D.).

[1] D. Torrent, W. J. Parnell, and A. N. Norris, Loss compensation in time-dependent elastic metamaterials, Phys. Rev. B **97**, 014105 (2018).
[2] G. Trainiti, Y. Xia, J. Marconi, G. Cazzulani, A. Erturk, and M. Ruzzene, Time-periodic stiffness modulation in elastic metamaterials for selective wave filtering: Theory and experiment, Phys. Rev. Lett. **122**, 124301 (2019).
[3] S. Lee, J. Park, H. Cho, Y. Wang, B. Kim, C. Daraio, and B. Min, Parametric oscillation of electromagnetic waves in momentum band gaps of a spatiotemporal crystal, Photonics Res. **9**, 142 (2021).
[4] D. L. Sounas and A. Alù, Non-reciprocal photonics based on time modulation, Nat. Photonics **11**, 774 (2017).
[5] Y. Wang, B. Yousefzadeh, H. Chen, H. Nassar, G. Huang, and C. Daraio, Observation of nonreciprocal wave propagation in a dynamic phononic lattice, Phys. Rev. Lett. **121**, 194301 (2018).
[6] S. P. Wallen and M. R. Haberman, Nonreciprocal wave phenomena in spring-mass chains with effective stiffness modulation induced by geometric nonlinearity, Phys. Rev. E **99**, 013001 (2019).
[7] H. Nassar, B. Yousefzadeh, R. Fleury, M. Ruzzene, A. Alù, C. Daraio, A. N. Norris, G. Huang, and M. R. Haberman, Nonreciprocity in acoustic and elastic materials, Nat. Rev. Mater. **5**, 667 (2020).
[8] T. Kitagawa, E. Berg, M. Rudner, and E. Demler, Topological characterization of periodically driven quantum systems, Phys. Rev. B **82**, 235114 (2010).
[9] J. Cayssol, B. Dóra, F. Simon, and R. Moessner, Floquet topological insulators, Phys. Status Solidi (RRL)—Rapid Research Lett. **7**, 101 (2013).
[10] Y.-T. Wang, Y.-W. Tsai, and W. Gao, Floquet topological photonic crystals with temporally modulated media, Opt. Express **28**, 21268 (2020).
[11] Y. Xiao, D. N. Maywar, and G. P. Agrawal, Reflection and transmission of electromagnetic waves at a temporal boundary, Opt. Lett. **39**, 574 (2014).
[12] K. Lee, J. Son, J. Park, B. Kang, W. Jeon, F. Rotermund, and B. Min, Linear frequency conversion via sudden merging of meta-atoms in time-variant metasurfaces, Nat. Photonics **12** (2018).
[13] Y. Zhou, M. Z. Alam, M. Karimi, J. Upham, O. Reshef, C. Liu, A. E. Willner, and R. W. Boyd, Broadband frequency translation through time refraction in an epsilon-near-zero material, Nat. Commun. **11**, 2180 (2020).
[14] F. Morgenthaler, Velocity modulation of electromagnetic waves, IRE Trans. Microwave Theory Tech. **6**, 167 (1958).
[15] J. T. Mendonça, A. Guerreiro, and A. M. Martins, Quantum theory of time refraction, Phys. Rev. A **62**, 033805 (2000).

[16] J. T. Mendonça and P. K. Shukla, Time refraction and time reflection: Two basic concepts, Phys. Scr. **65**, 160 (2002).
[17] J. T. Mendonça and A. Guerreiro, Time refraction and the quantum properties of vacuum, Phys. Rev. A **72**, 063805 (2005).
[18] B. W. Plansinis, W. R. Donaldson, and G. P. Agrawal, What is the temporal analog of reflection and refraction of optical beams, Phys. Rev. Lett. **115**, 183901 (2015).
[19] A. Akbarzadeh, N. Chamanara, and C. Caloz, Inverse prism based on temporal discontinuity and spatial dispersion, Opt. Lett. **43**, 3297 (2018).
[20] J. Gratus, R. Seviour, P. Kinsler, and D. A. Jaroszynski, Temporal boundaries in electromagnetic materials, New J. Phys. **23**, 083032 (2021).
[21] J. Zhang, W. R. Donaldson, and G. P. Agrawal, Temporal reflection and refraction of optical pulses inside a dispersive medium: An analytic approach, J. Opt. Soc. Am. B **38**, 997 (2021).
[22] D. M. Solís, R. Kastner, and N. Engheta, Time-varying materials in presence of dispersion: Plane-wave propagation in a Lorentzian medium with temporal discontinuity, arXiv: 2103.06142.
[23] F. Biancalana, A. Amann, A. V. Uskov, and E. P. O'Reilly, Dynamics of light propagation in spatio-temporal dielectric structures, Phys. Rev. E **75**, 046607 (2007).
[24] Y. Xiao, G. P. Agrawal, and D. N. Maywar, Spectral and temporal changes of optical pulses propagating through time-varying linear media, Opt. Lett. **36**, 505 (2011).
[25] C. Caloz and Z.-L. Deck-Léger, Spacetime metamaterials–part I: General concepts, IEEE Trans. Antennas Propag. **68**, 1569 (2020).
[26] C. Caloz and Z.-L. Deck-Léger, Spacetime metamaterials–part II: Theory and applications, IEEE Trans. Antennas Propag. **68**, 1583 (2020).
[27] V. Pacheco-Peña and N. Engheta, Antireflection temporal coatings, Optica **7**, 323 (2020).
[28] H. Li, A. Alù, and A. Alù, Temporal switching to extend the bandwidth of thin absorbers, Optica **8**, 24 (2021).
[29] V. Bacot, M. Labousse, A. Eddi, M. Fink, and E. Fort, Time reversal and holography with spacetime transformations, Nat. Phys. **12** (2016).
[30] M. Fink and E. Fort, From the time-reversal mirror to the instantaneous time mirror, Eur. Phys. J. Spec. Top. **226**, 1477 (2017).
[31] L. Lu, X. Ma, T. Dong, and Q. Liu, Time reflection and refraction in temporal periodic structures, in *2018 IEEE International Symposium on Antennas and Propagation & USNC/URSI National Radio Science Meeting, Boston* (2018), pp. 2253–2254, 10.1109/APUSNCURSINRSM.2018.8608800.
[32] D. Ramaccia, A. Toscano, and F. Bilotti, Light propagation through metamaterial temporal slabs: Reflection, refraction, and special cases, Opt. Lett. **45**, 5836 (2020).
[33] G. Castaldi, V. Pacheco-Peña, M. Moccia, N. Engheta, and V. Galdi, Exploiting space-time duality in the synthesis of impedance transformers via temporal metamaterials, Nanophotonics **10**, 3687 (2021).
[34] D. Ramaccia, A. Alù, A. Toscano, and F. Bilotti, Temporal multilayer structures for designing higher-order transfer functions using time-varying metamaterials, Appl. Phys. Lett. **118**, 101901 (2021).
[35] J. Zhang, W. R. Donaldson, and G. P. Agrawal, Impact of the boundary's sharpness on temporal reflection in dispersive media, Opt. Lett. **46**, 4053 (2021).
[36] R. Lifshitz, A. Arie, and A. Bahabad, Photonic quasicrystals for nonlinear optical frequency conversion, Phys. Rev. Lett. **95**, 133901 (2005).
[37] R. W. Boyd, *Nonlinear Optics*, 3rd ed. (Academic Press, New York, 2008).
[38] L. Ma, O. Slattery, and X. Tang, Single photon frequency up-conversion and its applications, Phys. Rep. **521**, 69 (2012).
[39] M. Lapine, I. V. Shadrivov, and Y. S. Kivshar, Colloquium: Nonlinear metamaterials, Rev. Mod. Phys. **86**, 1093 (2014).
[40] S. C. Wilks, J. M. Dawson, and W. B. Mori, Frequency up-conversion of electromagnetic radiation with use of an overdense plasma, Phys. Rev. Lett. **61**, 337 (1988).
[41] A. Nishida, N. Yugami, T. Higashiguchi, T. Otsuka, F. Suzuki, M. Nakata, Y. Sentoku, and R. Kodama, Experimental observation of frequency up-conversion by flash ionization, Appl. Phys. Lett. **101**, 161118 (2012).
[42] F. Miyamaru, C. Mizuo, T. Nakanishi, Y. Nakata, K. Hasebe, S. Nagase, Y. Matsubara, Y. Goto, J. Pérez-Urquizo, J. Madéo, and K. M. Dani, Ultrafast frequency-shift dynamics at temporal boundary induced by structural-dispersion switching of waveguides, Phys. Rev. Lett. **127**, 053902 (2021).
[43] B. Apffel and E. Fort, Frequency conversion cascade by crossing multiple space and time interfaces, Phys. Rev. Lett. **128**, 064501 (2022).
[44] B. L. Kim, C. Chong, S. Hajarolasvadi, Y. Wang, and C. Daraio, Dynamics of time-modulated, nonlinear phononic lattices, Phys. Rev. E **107**, 034211 (2023).
[45] See Supplemental Material at http://link.aps.org/supplemental/10.1103/PhysRevLett.133.077201 for determination and fitting of experimental parameters, full derivation of Snell and Fresnel relations, and experimental apparatus details and design considerations.
[46] T. Baba, Slow light in photonic crystals, Nat. Photonics **2**, 465 (2008).
[47] A. Cicek, O. Adem Kaya, M. Yilmaz, and B. Ulug, Slow sound propagation in a sonic crystal linear waveguide, J. Appl. Phys. **111**, 013522 (2012).
[48] J. Cha and C. Daraio, Electrical tuning of elastic wave propagation in nanomechanical lattices at MHz frequencies, Nat. Nanotechnol. **13**, 1016 (2018).
[49] P. Karki and J. Paulose, Stopping and reversing sound via dynamic dispersion tuning in a phononic metamaterial, Phys. Rev. Appl. **15**, 034083 (2021).
[50] J.-P. Groby, W. Huang, A. Lardeau, and Y. Aurégan, The use of slow waves to design simple sound absorbing materials, J. Appl. Phys. **117**, 124903 (2015).
[51] Q. Xu, P. Dong, and M. Lipson, Breaking the delay-bandwidth limit in a photonic structure, Nat. Phys. **3**, 406 (2007).

[52] Y. Lai, Y. Wu, P. Sheng, and Z.-Q. Zhang, Hybrid elastic solids, Nat. Mater. **10**, 620 (2011).

[53] C. Xu, G. Ma, Z.-G. Chen, J. Luo, J. Shi, Y. Lai, and Y. Wu, Three-dimensional acoustic double-zero-index medium with a fourfold degenerate Dirac-like point, Phys. Rev. Lett. **124**, 074501 (2020).

[54] N. Kruss and J. Paulose, Nondispersive one-way signal amplification in sonic metamaterials, Phys. Rev. Appl. **17**, 024020 (2022).

[55] S. Flach and A. Gorbach, Discrete breathers: Advances in theory and applications, Phys. Rep. **467**, 1 (2008).